J. Fluid Mech. (2024), *vol*. 988, A19, doi:10.1017/jfm.2024.426

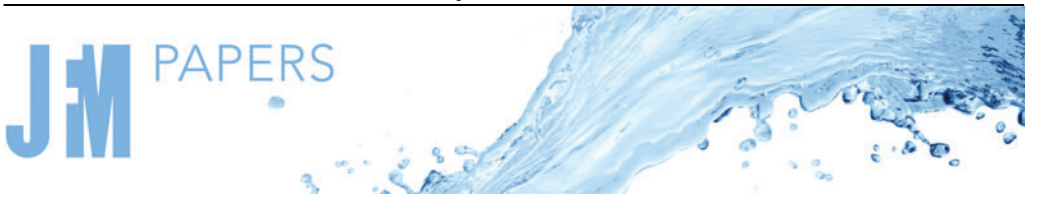

Rheological measurements and transition to turbulence for moderate Reynolds number inertial suspensions

Yichuan Song[1] **and Melany L. Hunt**[1,†]

[1]Division of Engineering and Applied Science, California Institute of Technology, Pasadena, CA 91125, USA

(Received 10 August 2023; revised 1 February 2024; accepted 25 April 2024)

Particulate flows at moderate particle Reynolds numbers are important in critical engineering and geological applications. This experimental study explores neutrally buoyant suspensions in an outer-rotating coaxial rheometer for solid fractions, ϕ, from 0.1 to 0.5, and particle Reynolds number, Re, from 0.5 to 800, covering laminar, transitional and turbulent regimes; Re is defined in terms of the square of the particle diameter and the shear rate. For $0.1 < \phi < 0.4$ and $0.5 < Re < 10$, the direct torque measurements normalised by the laminar flow torque, M/M_{lam}, are independent of Re, but depend on ϕ. For the same range of ϕ and for $10 < Re < 100$, the normalised torques depend on both ϕ and Re, and show an increasing dependence on Re. As Re increases, the flow transitions to turbulence. Small particles delay the turbulent transition for $\phi \leqslant 0.3$, while large particles augment the transition. A modified Reynolds number, Re', that depends linearly on the particle diameter and the maximum velocity, U_o, is introduced for both laminar and turbulent flows and shows a better correlation of the results as compared with Re. For $\phi = 50\,\%$, the normalised torque minus the torque at zero rotational speed is nearly independent of Re'. Rheological models based on Re' and the Krieger–Dougherty relative viscosity are proposed in the laminar regime for $10 < Re' < 500$; in the turbulent regime, a correlation is proposed in terms of Re' and ϕ for $1000 < Re' < 6000$.

Key words: suspensions, particle/fluid flow

1. Introduction

Many prior studies have investigated the rheological behaviour of non-Brownian, hard-particle flows at low particle Reynolds numbers (Batchelor 1970; Larson 1999; Stickel & Powell 2005). These studies typically define the particle Reynolds number using

† Email address for correspondence: hunt@caltech.edu

the shear rate of the flow, $\dot{\gamma}$, and the square of the hard-particle diameter, d, such that $Re = \dot{\gamma}\rho d^2/\mu$ where ρ represents the fluid density and μ represents the fluid dynamic viscosity. For $Re < 1$, the stresses behave in a Newtonian manner with the shear stress, τ, which depends on the effective viscosity of the liquid–solid flow, μ_e, such that $\tau = \mu_e\dot{\gamma}$; the ratio of the flow effective viscosity to the fluid dynamic viscosity is the relative viscosity, $\mu_r = \mu_e/\mu$. Under dilute conditions, typically $\phi < 0.05$, the particles are spaced far enough apart that the particulate flow is not influenced by the other particles; hence, the relative viscosity is only dependent on the suspension solid fraction, $\mu_r = 1 + 2.5\phi$ (Larson 1999). At higher solid fractions, the hydrodynamic interactions between particles increase, which results in an increase in particle stress, and the relative viscosity shows an increased dependence on the solid fraction. Several semi-empirical relations have been introduced, such as the Eilers and the Krieger–Dougherty (KD) relative viscosity models or the more recent expression by Boyer, Guazzelli & Pouliquen (2011). The relative viscosity expressions depend on the maximum solid fraction for a sheared suspension, ϕ_m. As ϕ approaches ϕ_m, the relative viscosity is sensitive to minor changes in solid fraction and the models predict some differences in μ_r (Stickel & Powell 2005; Boyer *et al.* 2011).

Beyond low-Reynolds-number suspensions, there are many industrial and geological scenarios in which inertial effects become important. Examples include the processing of biomass slurries (Stickel *et al.* 2009) with particles from micrometres to millimetres, rapid debris flows involving soil, clays and rocks (Iverson 2012), and transport of proppant slurries in hydraulic fracturing applications (Osiptsov 2017). Compared with low-Reynolds-number suspensions, there is sparse experimental data involving moderate Reynolds numbers. Hence, additional experimental measurements on moderate-Reynolds-number suspensions are crucial in modelling and validating the relationships.

Figure 1 shows a regime map in terms of the particle Reynolds number, Re, and the suspension solid fraction, ϕ; the experimental studies considered rheological properties of neutrally buoyant suspensions. The map does not include the many prior studies for suspensions in which particle Reynolds numbers are negligible with $Re < 10^{-3}$. The map includes two non-Brownian experimental studies at slightly higher Reynolds number ($10^{-3} < Re < 0.1$). One is the experiments by Acrivos, Fan & Mauri (1994) involving particles that are 0.13 mm, larger than the particle size typically used in experiments of suspensions. Their results show shear thinning behaviour, which the authors attribute to particle settling caused by a slight mismatch (less than 3 %) in the fluid and particle densities. By accounting for the settling, the measured effective viscosities compare well with relationships at low Re. Experiments conducted by Boyer *et al.* (2011) cover the rheological transition from a suspension to a granular flow. Although the study used relatively large particles (0.58 and 1.1 mm), the Reynolds numbers are small due to the highly viscous suspending fluid. Their results are consistent with relative viscosity models such as Eilers and KD. Other recent experiments investigate the impact of particles on Taylor–Couette flows (Majji & Morris 2018; Ramesh, Bharadwaj & Alam 2019; Dash, Anantharaman & Poelma 2020; Moazzen *et al.* 2022); although some of these studies include torque measurements, the focus of the investigations involves the impact of particles on the transition process.

At higher Re, the map includes one set of experiments by Bagnold (1954) and the experimental study by Tapia *et al.* (2022). A prior analysis of the Bagnold experiments showed that the design of the rheometer and the conditions under which it was operated created secondary flows that increased the measurements of stress significantly (Hunt *et al.* 2002). The critical flow parameter, often referred to as the Bagnold number, marked the

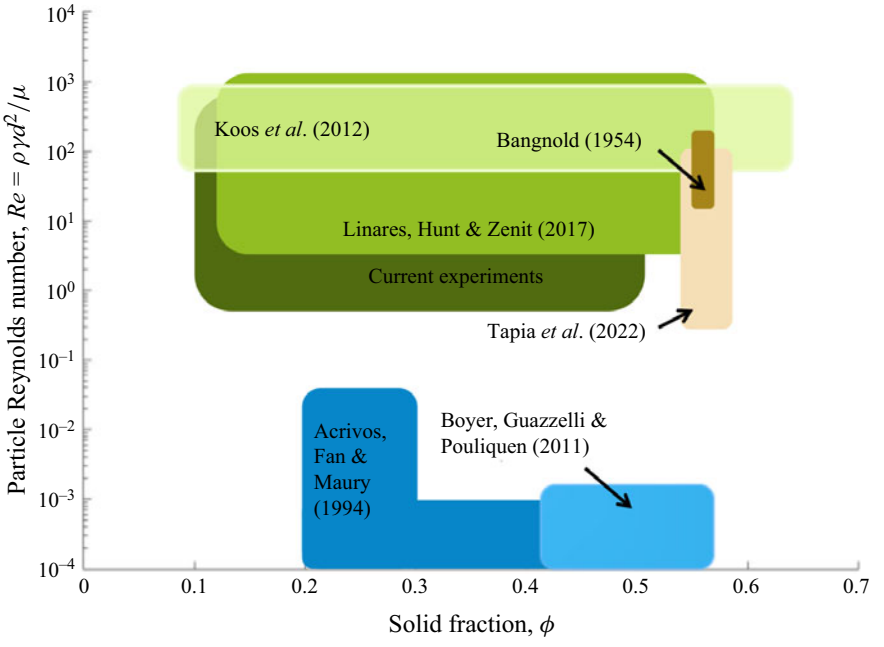

Figure 1. Regime map of experimental studies for rheological properties of neutrally buoyant dense suspensions in terms of particle Reynolds number, Re, and solid fraction, ϕ.

change from a simple shear flow to an azimuthal flow with end-plate vortices; hence, the transition was not caused by the inertial effects of the particles. In the regime map, only one set of experimental measurements at $\phi = 0.56$ is included, which was done at Reynolds numbers low enough that the secondary flows did not impact the rheological measurements. The experiments by Tapia *et al.* (2022) involve flows in a constant-volume parallel plate rheometer for ϕ from 0.52 to 0.58 and flows with a constant normal stress for ϕ from 0.54 to 0.62. At low Reynolds numbers, the measurements are consistent with models based on effective viscosity. At the highest rotational speeds, the torque shows an increasing dependence on the speed; however, flows in a parallel-plate rheometer can also develop secondary flows beyond a critical speed (Ellenberger & Fortuin 1985; Hunt & Zenit 2024).

The other studies in the figure involve prior work at Caltech (Koos *et al.* 2012; Linares, Hunt & Zenit 2017) using the same outer-rotating rheometer; with this type of rheometer, Re measurements for circular Couette flow extend to a higher range as compared with a rheometer with an inner rotating cylinder. Both of these prior studies focused on measuring the shear stress for neutrally buoyant suspensions under conditions in which inertial effects are important. The study by Koos *et al.* (2012) covered Re from 18 to 780 for ϕ from 0.077 to 0.64 and involved particles of different shapes and sizes. In the study, the normalised torques were independent of Re; this result was surprising. Based on particle velocity measurements near the inner stationary wall of the rheometer, it was found that the smooth walls resulted in considerable particle slip (Barnes 1995). Although the torque magnitude increased with solid fraction, the torques could be modelled with an effective viscosity even at high Reynolds numbers. The more recent study by Linares *et al.* (2017) considered a wider range of Reynolds numbers and introduced roughness by gluing particles to the rheometer walls; the glued particles were of the same size as the particles

used in the suspension. Those experiments used a single particle size and two fluids of different viscosity. For the more viscous interstitial fluid covering $3 < Re < 80$, the relative viscosity increased with Re for $\phi = 0.1$ to 0.3. At higher solid fractions, the data showed some shear thinning behaviour. For the less-viscous fluid with $80 < Re < 1000$, the data showed that the normalised torque increases with Re; most data in this Re regime corresponded with conditions in which the suspensions had transitioned to turbulence.

Although not shown in the regime map, several simulations studied the viscous and the inertial effects in neutrally buoyant particulate flows to determine the total stress in terms of ϕ and Re (Kulkarni & Morris 2008; Picano *et al.* 2013; Yeo & Maxey 2013; Haddadi & Morris 2014; Rahmani, Hammouti & Wachs 2018; Zhou & Prosperetti 2020; Yousefi *et al.* 2023). The recent paper by Zhou & Prosperetti (2020) summarises these numerical studies, which cover ϕ from 0.05 to 0.38 and particle Reynolds number from 0.02 to 40. These particle-resolved simulations involve different numerical methods, different boundary conditions, varying numbers of particles and different sizes of shear cells. The properties are calculated by averaging the stresses over a representative volume that includes fluid and solid phases. These simulations are valuable in understanding the different contributions to the overall stresses, including the suspension stresslet, the Reynolds stresses in the flow, as well as the particle acceleration (Batchelor 1970; Kulkarni & Morris 2008; Zhou & Prosperetti 2020). The results show that for shear flows with neutrally buoyant suspensions, the relative viscosity begins to increase in comparison with the low-Reynolds-number results as the Re increases above one. As found in Rahmani *et al.* (2018), the particle phase stress increases with particle Reynolds number and solid fraction; at $Re = 20$ and $\phi = 30\,\%$, the particle phase shear stress plays a dominant role because of the shearing of the liquid in the small spaces between particles, whereas the Reynolds stresses and the contact forces do not contribute significantly. The work by Zhou & Prosperetti (2020) also includes the contributions from particle collisions, which becomes important as the inertia is increased.

The current study aims to further extend the experimental Reynolds number measurement to previously untested Re regions. The experiments involve two different sizes of particles with spherical and nearly spherical shapes in millimetre scale and two different fluids with varying viscosities. The experimental measurements show that the traditional Re used in shear flows of suspensions, Re, which depends on d^2, may not be the best scaling variable to correlate the moderate-Reynolds-number measurements. As an improvement, the current results are presented in terms of the newly proposed Reynolds number, Re', which is based on the maximum liquid–solid flow velocity, and linearly on the diameter of the particle. Although Re' is not typically used in sheared suspension studies, it is the Reynolds number most commonly used to examine the flow field and drag on an isolated sphere. As the inertia of the flow increases, velocity fluctuations and velocity differences between the solid and liquid phases are expected to impact the suspension stresses. As a result, this paper proposes rheological models using Re' and ϕ and presents a comparison with recent simulations found in the literature.

2. Experimental methods

The Caltech coaxial rheometer is designed to study liquid–solid flows with millimetre-sized particles for conditions spanning laminar to turbulent flows. Prior studies have used the same rheometer, as found in Koos *et al.* (2012) and Linares *et al.* (2017). Relative to the prior studies, the current instrumentation has been upgraded to improve the experimental repeatability and measurement accuracy using a new data acquisition (DAQ)

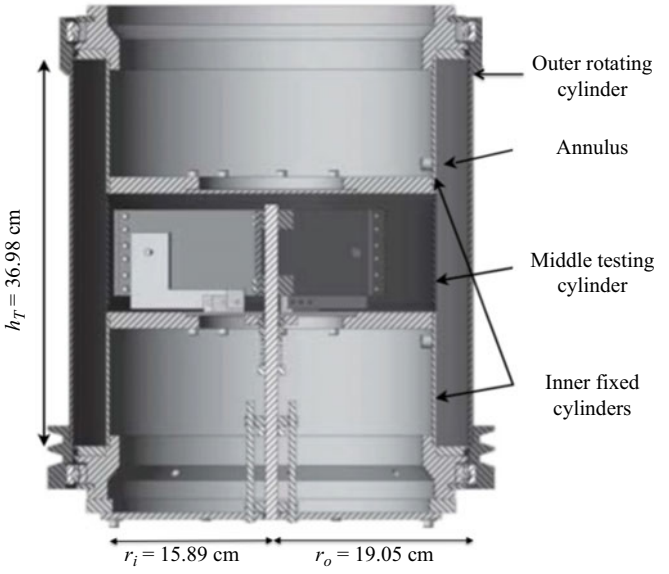

Figure 2. The outer-rotating Caltech coaxial rheometer. The rheometer and the dimensions are shown without the roughened surfaces. The schematic is from Linares *et al.* (2017).

system including reaction torque sensors. In addition, pure fluid experiments are conducted over five fluid viscosities; the suspension experiments involve two fluid viscosities and two sizes of neutrally buoyant particles to increase the *Re* regime (Song 2022).

Figure 2 presents the schematic for the Caltech coaxial rheometer consisting of an outer-rotating cylinder and fixed inner cylinder. The outer rotating drum is connected to an electric motor by a rubber belt. The electric motor driving the outer cylinder has nine levels of rotational speed. There are three inner subcylinders: the free-rotating middle measurement cylinder and the top and the bottom fixed subcylinders. Both the bottom and the top subdrums are stationary to reduce the impact of secondary flows from the corners (Hunt *et al.* 2002). The middle measurement cylinder of height, $H = 0.11$ m, measures the torque of the suspension. A central shaft supports the middle measurement cylinder so that it can rotate freely; there are gaps of approximately 1 mm between the measurement cylinder and the upper and lower stationary cylinders to allow the middle subcylinder to rotate freely and to prevent the entrance of particles sheared in the annulus. A calibrated reaction torque sensor installed above the rheometer constrained the middle measurement cylinder. Ball bearings are installed between the outer drum and the stationary inner subcylinders to facilitate the rotation. The particulate flows in the rheometer annulus are sheared by the rotational outer cylinder. The current experimental design allows the real-time direct torque measurement at the middle measurement cylinder without subtracting the bearing friction or other ancillary fluid losses, as has been done in other studies (Bagnold 1954; Savage & McKeown 1983). The DAQ system including reaction torque sensors replaced the prior system that used springs attached to the central shaft of the rheometer (Koos *et al.* 2012; Linares *et al.* 2017). The torque measurements ranged from 0.01 to 5.6 N m with a resolution of the torque sensor of 0.0014 N m. The range of the measured shear stress is from 0.54 to 302 Pa.

The upper guard cylinder and the middle measurement cylinder can also be removed and replaced with a transparent inner cylinder. This transparent cylinder allowed for

visualisation of the flow, especially for particles close to the inner cylinder, which can be recorded using a high-speed camera (Song 2022). Observations of the flow for a range of flow conditions showed an overall tangential movement of the particles with no large-scale toroidal motion.

The current experiments use two types of particles: polystyrene spheres with an average diameter $d = 1.27 \pm 0.01$ mm for $b/d = 19.6$ and density $\rho = 1050$ kg m^{-3} and nearly spherical styrene acrylonitrile (SAN) particles with an effective diameter $d = 3.22 \pm 0.02$ mm for $b/d = 7.73$ and $\rho = 1050$ kg m^{-3}. For the neutrally buoyant experiments at 20 °C, the study uses a 18 % glycerol–water mixture ($\mu = 1.84 \times 10^{-3}$ N s m^{-2}) and a higher-viscosity 51 % glycerol–ethanol mixture ($\mu = 2.90 \times 10^{-2}$ N s m^{-2}) (Ernst, Watkins & Ruwe 1936; Cheng 2008). Elliptical polystyrene particles with an effective diameter of 3.34 mm are used to roughen the surface walls to reduce particle slip near wall surfaces. The elliptical particles are glued on the thin vinyl sheets, which cover the annulus surface. With roughness, the annulus dimensions are $r_o = 18.72$ cm and $r_i = 16.22$ cm giving a gap width of $b = r_o - r_i = 2.49$ cm.

The rotational speed, ω, is measured by a laser sensor that detects the light reflected off eight targets equally spaced on the outer cylinder surface. The rotational speed is used to determine the shear rate at the inner cylinder with $\dot{\gamma} = 2\omega {r_o}^2/({r_o}^2 - {r_i}^2)$. The rotational speed of the motor ranged from approximately 1.3 to 16 rad s^{-1} with shear rates from 10 to 130 s^{-1}. There is some variation in the minimum speed to operate under steady-state conditions due to the varying rotational friction caused by the different solid fractions of the particulate flow. To ensure that the torque is large enough to be measured accurately by the torque sensor, the minimum shear rate was approximately 15 s^{-1} for the l0 % solid fraction in the low-viscosity liquid. At low speeds and 50 % solid fraction, the shearing of the packed bed caused the bed to dilate, creating an increase in stress on the walls. For steady-state operation, it was not possible to operate the motor at the lowest speeds; this issue was more pronounced for the larger SAN particles. Hence, the minimum value of the shear rate increased to approximately 33 s^{-1} for low-viscosity fluid and 23 s^{-1} for the high-viscosity fluid for $\phi = 0.5$.

The torque measurements are made under steady-state conditions with each data point averaged over at least five individual experimental measurements. For each experimental measurement set for either a pure fluid or a suspension, the measurements are taken under both conditions in which the rotational speed is increased from the lowest to the highest setting and the rotational speed is decreased from the highest to the lowest speed setting. For the same pure fluids or particulate flow set-up, the torque measurements with either increasing or decreasing rotational speed are repeatable at the specified shear rate. The liquid density and the fluid temperature were recorded to determine the fluid properties. To ensure the suspensions are neutrally buoyant, the fluid temperature is monitored and controlled throughout the experiment. The error bars presented in this study correspond to the standard deviations of the normalised torque in the experiment, as well as the measurement uncertainty. The largest uncertainties are at lower shear rates due to variations in the motor rotational speed and the limitation of torque sensor resolution that led to larger error bars at lower Reynolds numbers.

3. Pure fluids measurements and transition to turbulence

The first set of experiments involves torque measurements for liquids without particles using the rheometer with roughened inner and outer walls. The experiments using pure fluids extend the torque measurements in the Caltech outer-rotating rheometer to

previously untested gap Reynolds numbers (Re_b) regime and provide a test case for the measurement accuracy; the experiments also determine the conditions under which the flow transitions to turbulence. The experiments use five different fluids including pure water, water–glycerol mixtures and an ethanol–glycerol mixture spanning viscosities from 1.00×10^{-3} N s m^{-2} to 6.72×10^{-2} N s m^{-2} for fluid properties under 20 °C.

Figure 3 shows the direct torque measurement, M, normalised by the torque considering a laminar flow, M_{lam}, with respect to gap Reynolds number, $Re_b = \rho\omega r_o b/\mu$, depending on the annular gap width, $b = r_o - r_i$. The values of Re_b span from 300 to 8×10^4. The theoretical laminar torque is computed using, $\dot{\gamma}$, the shear rate at the inner cylinder (Schlichting 1951):

$$M_{lam} = 2\pi\mu H {r_i}^2 \dot{\gamma}. \tag{3.1}$$

As found in the figure for liquid mixtures of the 51 % glycerol–ethanol and 77 % glycerol–water, the torque ratios, M/M_{lam}, are close to 1, which are consistent with the theoretical laminar flow; the torque measurements at the lowest shear rate are close to the resolution of the reaction torque sensors, which increases the measurement uncertainty. The measurements of the 50 % water–glycerol mixture cover a Re_b range from 3.69×10^3 to 1.19×10^4 and span the laminar–turbulent transition. The normalised torque begins to deviate from the theoretical laminar value around $Re_b \approx 6.5 \times 10^3$, which is smaller than the value found by Koos *et al.* (2012) using smooth walls and a slightly larger gap. The fully turbulent Reynolds number is $Re_b \approx 1.1 \times 10^4$, which is consistent with other studies (Taylor 1936*a*,*b*; Coles 1965; Linares *et al.* 2017). Figure 3 shows the experimental values of the critical Re_b and the fully turbulent Re_b. The figure also presents the data for water and the fluid mixture of 28 % glycerol/72 % water with Re_b ranges of 6.02×10^3–3.17×10^4 and 1.33×10^4–7.49×10^4. The majority of measurements are beyond the critical Re_b. Experimental results were repeated multiple times; results were unchanged independent of an increase or decrease of the speed between data points.

For an outer rotating cylinder at low speeds, the flow is an azimuthal laminar flow including weak Ekman vortices caused by the no-slip conditions at the stationary end plates (Coles & VanAtta 1966; VanAtta 1966; Linares *et al.* 2017). As the rotational speed is increased, the strength of the vortices increases and turbulence begins to develop at the corners of the annulus with the breakdown of the vortices (VanAtta 1966; Ravelet, Delfos & Westerweel 2010; Linares *et al.* 2017). As a result, turbulence can form at the corner and not be detected by the middle testing subcylinder until the turbulent flow fills the entire annulus (see figure 2). The transition to turbulence contributes significantly to the measured torque. The sudden rise of M/M_{lam} is similar to observations of the intermittent turbulent regions and catastrophic transition as described by VanAtta (1966). The M/M_{lam} measurements for pure water and the mixture of the 28 % glycerol/72 % water compare well beyond the critical Re_b. At the highest rotational speed, the M/M_{lam} value for the fluid mixture of the 28 % glycerol/72 % water is roughly 18 times larger than the value of the laminar flow. At the maximum rotational speed, the M/M_{lam} value for pure water is roughly 31 times larger than the value of the laminar flow. For Re_b of 6.02×10^3, there exists an outlier measurement point for the 28 % glycerol/72 % water results with normalised torque substantially higher than the corresponding 50 % glycerol–water measurement. This observation of both laminar and turbulent states at the same Reynolds number is consistent with the experiments by Coles (1965) and by VanAtta (1966) on flow hysteresis in Taylor–Couette systems. Presumably, the data for the 28 % glycerol/72 % water mixture could relaminarise at lower Reynolds numbers provided that the speed of the motor could be decreased further. The results in the fully turbulent regime

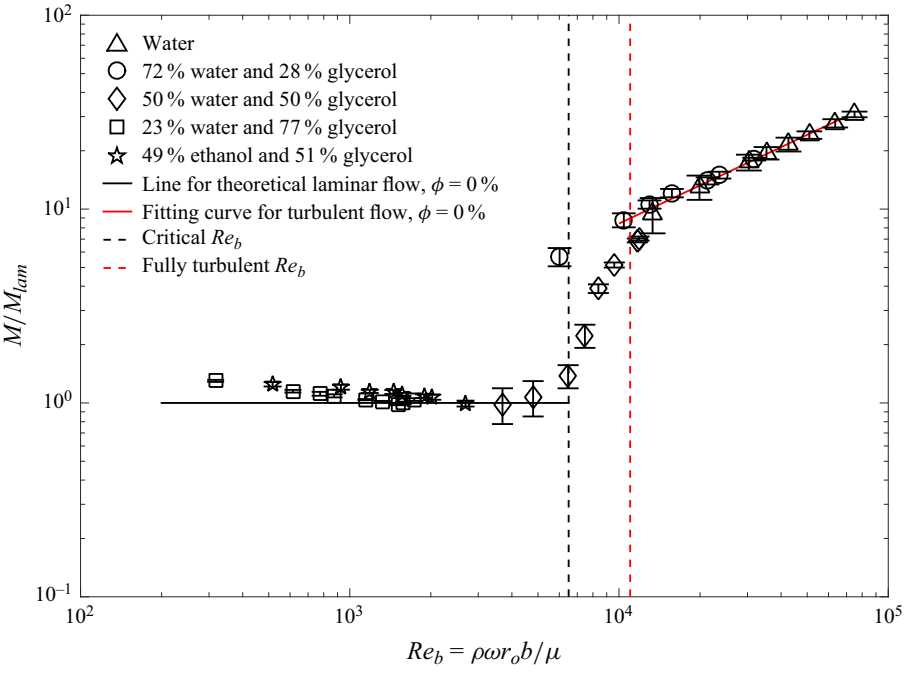

Figure 3. The ratio of the direct measurement of the torque, M, to the laminar torque, M_{lam}, with respect to the gap Reynolds number, Re_b, for water, the 51 % glycerol–ethanol mixture, and the 28 %, 50 %, 77 % glycerol–water mixtures. The solid line in black corresponds to the theoretical laminar value of M/M_{lam} considering smooth walls. The dashed line in black represents the critical Re_b. The dashed line in red corresponds to the fully turbulent Re_b. The solid line in red is the fitting curve ($M/M_{lam} = 0.020{Re_b}^{0.66}$) for the turbulent measurements.

are best fit using the equation $M/M_{lam} = 0.020{Re_b}^{0.66}$; hence, the torque for turbulent flow increases with the shear rate to the 1.66 power, $M \propto \dot{\gamma}^{1.66}$, similar to that found in the earlier study by Linares *et al.* (2017).

4. Rheological measurements and transition to turbulence

To investigate the effects of increasing fluid and particle inertia on the rheological properties, the torque measurements were made over a range of Reynolds numbers using neutrally buoyant particles with two different sizes, a 1.27-mm polystyrene particle and a 3.22-mm SAN particle, and using two different fluid viscosities, an 18 % glycerol–water fluid mixture (GW) and a 51 % glycerol–ethanol (GE) fluid mixture. Figure 4 presents the direct torque measurements normalised by the theoretical laminar torque in terms of M/M_{lam} for both sets of polystyrene and SAN particles immersed in the higher-viscosity fluid with respect to Re_b for solid fractions = 0.1, 0.2, 0.3, 0.4 and 0.5, covering a Re_b range from 186 to 3.08×10^3; the figure also includes the pure fluid result at the laminar state. The gap Reynolds numbers for both particles are below the critical Re_b for pure fluids. Since the direct measurement for this experimental study is torque, the results are presented as the torque ratio, M/M_{lam}, instead of relative viscosity, μ_e/μ. When inertial effects are negligible, the torque ratio is equivalent to the low-Reynolds-number relative

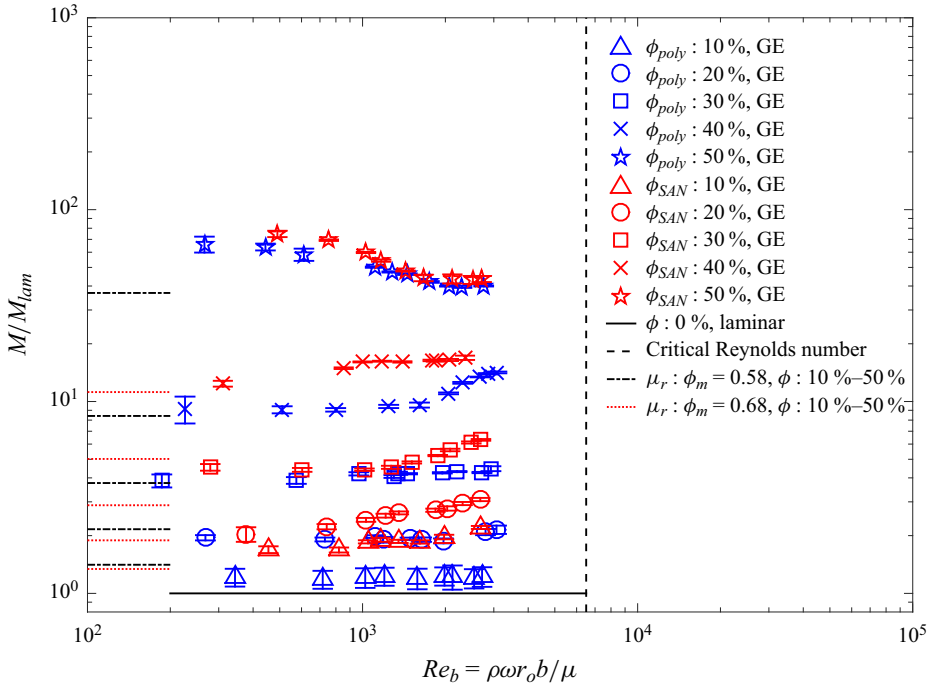

Figure 4. The ratio of experimental torque measurements, M, to the torque of laminar flow, M_{lam}, with respect to Re_b, for large SAN particles and small polystyrene particles suspending in the 51 % glycerol–ethanol fluid mixture for ϕ from 10 % to 50 %. The black dash-dotted lines correspond to μ_r values using $\phi_m = 0.58$ and ϕ from 10 % to 50 %. The dotted lines in red correspond to μ_r values using $\phi_m = 0.68$ and ϕ from 0.1 to 0.5.

viscosity assuming a homogeneous distribution of particles,

$$M/M_{lam} = \mu_e/\mu \quad \text{as} \quad Re \to 0. \tag{4.1}$$

There are several models for the relative viscosity. The KD model is a function of the ratio of ϕ to the maximum shearable solid fraction, ϕ_m, as follows:

$$\mu_e/\mu = \mu_r(\phi, \phi_m) = (1 - \phi/\phi_m)^{-a}. \tag{4.2}$$

The exponent, a, is often related to the product of the intrinsic viscosity, $[\eta]$, and ϕ_m such that $a = [\eta]\phi_m$ with $[\eta] = 2.5$ for spheres (Larson 1999; Stickel & Powell 2005). Here a is fixed at $a = 1.82$, a value that has been used in other neutrally buoyant suspension experiments (Matas, Morris & Guazzelli 2003; Linares *et al.* 2017). The values of μ_r are found in table 1 for $\phi_m = 0.58$ and $\phi_m = 0.68$.

For the solid fractions of 10 %, 20 %, 30 % and 40 %, the M/M_{lam} values of the polystyrene particles are constant until $Re_b \approx 2.2 \times 10^3$, and then the ratios increase slightly for $2.2 \times 10^3 < Re_b < 3 \times 10^3$. For the same range of Re_b, the M/M_{lam} values considering the larger SAN particles show an increased dependence on Re_b; the SAN measurements are roughly 80 %, 48 % and 47 % larger than the measurements of the small particles at the largest rotational speed for $\phi = 0.1$, 0.2 and 0.3. For $\phi = 0.1$, the SAN measurements are greater than the polystyrene measurements for all Re_b. For $\phi = 0.4$, the SAN measurements show some increase as Re_b increases, but the results then show a plateau. For $\phi = 0.4$ and Re_b around 2.3×10^3, the SAN measurements are approximately 35 % greater than the polystyrene measurements.

ϕ	$\mu_r(\phi, 0.58)$	$\mu_r(\phi, 0.68)$	a_1	a_2	r.m.s. Re	b_1	b_2	r.m.s. Re'
10 %	1.41	1.34	0.70	0.21	0.54	0.0033	−0.23	0.17
20 %	2.16	1.89	0.70	0.21	0.37	0.0031	−0.07	0.20
30 %	3.76	2.88	0.37	0.39	0.96	0.0067	−0.06	0.40
40 %	8.41	5.02	0.67	0.39	4.55	0.043	−2.40	2.91
50 %	36.8	11.2	—	—	—	—	—	—

Table 1. Summary of the KD relative viscosity model and the fitting results of the measurements before the turbulent transition. The fitting results presented in figure 6 correspond to the Re region from 10 to 100. The fitting models presented in figure 7 correspond to Re' from 100 to 400.

Figure 4 also includes (on the left-hand side of the image) the values of μ_r for $\phi_m = 0.58$ and 0.68, which do not depend on Re_b. For $\phi = 0.3$ and 0.4, the M/M_{lam} values for the small polystyrene particles at the lowest values of Re_b correspond well with μ_r for $\phi = 0.58$. For $\phi = 10\,\%$ and 20 %, the M/M_{lam} values correspond better with μ_r using $\phi_m = 0.68$, although the measurement for $\phi = 10\,\%$, are lower than that value. The difference appears to be linked to the roughness of the walls, which is considerably larger than the polystyrene particles. As a result, the polystyrene particles are small enough to become trapped in the interstices of the larger wall particles. Hence, the number of small particles in the central region of the rheometer decreases and the solid fraction for the bulk of the flow is lower, leading to a smaller torque and a decreased effective viscosity. Therefore, the ratio ϕ/ϕ_m using $\phi_m = 0.58$ is too large for the polystyrene particles. The issue of trapped particles is less significant for $\phi \geqslant 0.2$ and for the polystyrene particles in the less-viscous glycerol–water mixture.

The results for the 50 % solid fraction show a decrease in M/M_{lam} as Re_b increases for both sizes of particles with slightly larger values for SAN particles than for smaller polystyrene particles. Overall, for $\phi = 50\,\%$, the SAN and the polystyrene measurements compare well and show similar trends for gap Reynolds numbers up to $Re_b = 2.7 \times 10^3$ in contrast with the other solid fractions. In terms of μ_r, the data at the highest values of Re_b compare best with the value of μ_r for $\phi = 0.58$. As explained in § 2, the experiments for $\phi = 50\,\%$ were not conducted at the lowest motor rotational speed because the torque provided by the motor was not sufficient to overcome the stress imparted by the particles on the confining walls while maintaining a constant rotational speed. Similar observations were also made by Savage & McKeown (1983) for an inertial suspension with a rotating inner cylinder for $\phi > 0.5$. They concluded that in a narrow-gap, annular rheometer with rough, rigid walls, the high-solid-fraction suspension could not dilate sufficiently when sheared at low speed. The authors speculated that there were groups of particles that remain locked together, especially near the stationary wall, with the shearing of particles confined to a smaller zone near the moving wall. Under these conditions, the assumption of a homogeneous distribution of particles may not be representative of the actual flow conditions.

In looking at the raw data of M vs ω for $\phi = 0.5$, a linear extrapolation to $\omega = 0$ gives a non-zero value of torque, M_o, which is larger than the resolution of the torque sensor. For the other solid fractions, a similar extrapolation approaches zero or is below the sensor resolution (Song 2022). Under conditions in which $M_o \neq 0$, the flows behave similarly to a yield stress fluid or Bingham fluid in which the imposed torque needs to be large enough to shear the suspension across the full width of the rheometer gap (Young, Shetty & Hunt 2024). For $\phi = 0.5$, the torque value at zero shear rate, M_o, is estimated using

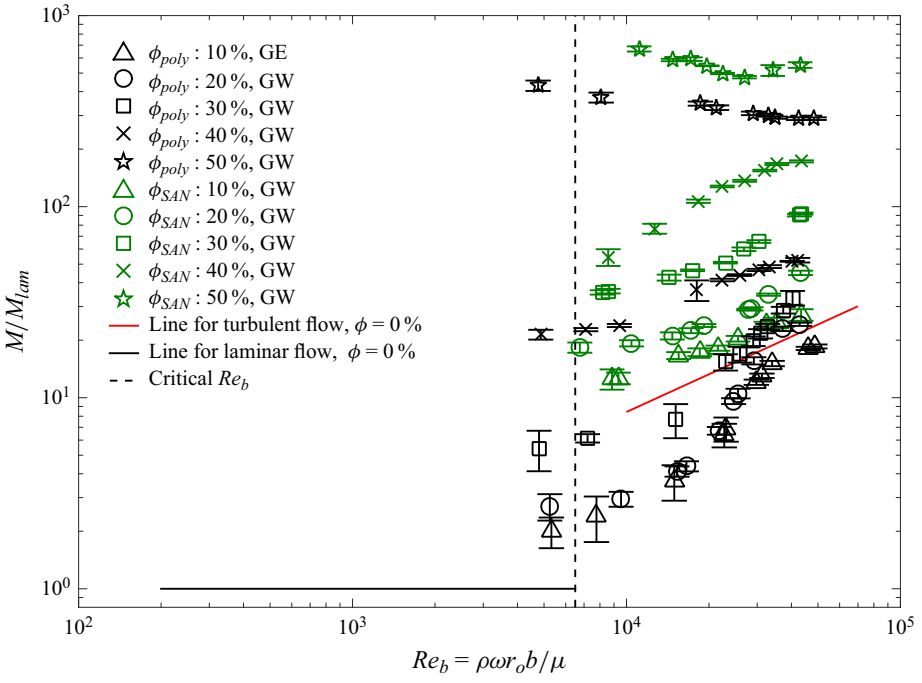

Figure 5. The ratio of experimental torque measurements, M, to the torque of laminar flow, M_{lam}, with respect to Re_b, considering large SAN particles and small polystyrene particles suspending in the fluid mixture of 18 % glycerol and 82 % water for ϕ from 10 % to 50 %.

fits to the raw torque vs rotational speed data and extrapolating to the origin. The data for $\phi = 0.5$ is presented in terms of $M - M_o$ in later figures. As a note, the work by Savage & McKeown (1983) cannot be used to find a torque at zero shear because those authors subtract off friction and other ancillary fluid contributions that are part of their gross torque measurements; as a result, an extrapolation of their measurements to $\omega = 0$ gives a negative value of M_o. Because the torque is measured directly in the current work, it is possible to estimate M_o at the highest solid fractions. In related experiments by Boyer *et al.* (2011), the shear stress as rotational speed decreases to zero is also non-zero. In that study, the authors imposed a normal stress and looked at the transition from a static granular bed to a shearing suspension; the shear stress at zero shear is equated to a friction factor and the normal stress.

Figure 5 presents similar measurements for both sphere sizes in the fluid mixture of 18 % glycerol/82 % water for solid fractions from 0.1 to 0.5, covering a Re_b range from 4.8×10^3 to 4.9×10^4. The laminar and turbulent fitting curves and the critical Re_b for pure fluids are also shown. Using Re_b, the results extend from before the critical Re_b considering pure fluids to the fully turbulent state. For $Re_b < 3 \times 10^4$, the polystyrene measurements for $\phi = 10$ %, 20 % and 30 % lie below the line correlating the turbulent data for pure fluids and have a shallower slope, indicating that the small polystyrene particles suppress the turbulent transition. Conversely, the 10 %, 20 % and 30 % data for the larger SAN particles fall above the pure fluid correlations, indicating the large SAN particles augment the transition and increase the torque for the same value of Re_b as compared with the results for the smaller particles. At $Re_b \approx 4.2 \times 10^4$, the M/M_{lam} values for the larger SAN particles are 50 %, 86 % and 180 % greater than the M/M_{lam}

values for the smaller polystyrene particles for solid fractions of 0.1, 0.2 and 0.3. The criterion to determine whether the liquid–solid flow becomes turbulent does not depend solely on whether the normalised torque of suspension exceeds the line correlating the turbulent data sets for pure fluids. Instead, it depends on the comparison of the trend of turbulent data sets for liquid–solid flow and the slope of the turbulent data points for pure fluids.

For 40 % and 50 % solid fractions, the measurements for both sizes of particles are above the pure fluid line. For 40 % solid fraction, the results for both particles show an increase in the normalised torque as Re_b increases with the large particle measurements being 230 % larger than the small polystyrene measurements at $Re_b \approx 4.2 \times 10^4$. For $\phi = 0.5$, the M/M_{lam} values for SAN results decrease first until $Re_b < 2.70 \times 10^4$, then show a slight increase for Re_b from 2.7×10^4 to 4.3×10^4. The 50 % polystyrene results decrease over the tested Reynolds number region; the measurements are roughly 48 % smaller as compared with the SAN measurements at the highest Re_b. For both sizes of particles, the values of M_o are non-zero.

The impact of the hard spheres on the turbulent transition has been considered in pipe flow, such as the studies by Matas *et al.* (2003), Yu *et al.* (2013) and Leskovec, Lundell & Innings (2020). For particles much smaller than the diameter of the pipe, the small particles attenuate the turbulence; for larger particles, the particles may enhance the turbulent effects depending on the solid fraction. For Taylor–Couette flows, recent experiments (Majji & Morris 2018; Ramesh *et al.* 2019; Dash *et al.* 2020; Moazzen *et al.* 2022) looked at the effects of particles on the presence of Taylor vortices and the subsequent bifurcations. As described by Moazzen *et al.* (2022), there are differences in the laminar to turbulence thresholds in Taylor–Couette flows as compared with those found in pressure-driven flows. The data compiled over a wide range of parameters as found by Moazzen *et al.* (2022) demonstrates that the gap size to particle diameter ratio can affect the order of the flow transitions and the particles can also create new flow states as compared with flows of pure fluids.

In the current studies, small polystyrene particles for $\phi < 0.3$ increase μ_e, decreasing the effective Reynolds number, and leading to the delay of turbulent transition (Balachandar & Eaton 2010). The presence of large SAN particles should also increase the effective viscosity of the particulate flow, but SAN particles may be large enough to also enhance the velocity fluctuations, leading to the increased normalised torque (Cartellier & Riviere 2001; Mendez-Diaz *et al.* 2013). As compared with the laminar–turbulent transition using pure-fluid measurements in figure 3, the measurements for the polystyrene particles with $\phi = 0.1$, 0.2 or 0.3 show a smoother transition, which is consistent with prior studies on liquid–solid flows (Lashgari *et al.* 2014; Agrawal, Choueiri & Hof 2019). As discussed in regard to the pure fluid measurements in the transition region, it is possible to find both laminar and turbulent states at the same Reynolds number.

Figures 6 and 7 present the normalised torque data considering ϕ ranging from 0.1 to 0.4 for data points that are below pure-fluid fully turbulent regime Reynolds number ($Re_b < 1.1 \times 10^4$); these data sets include small polystyrene particles in the glycerol and ethanol mixture (data sets in blue), some of the polystyrene measurements (data sets in black) in the glycerol and water mixture, and the large SAN measurements (data sets in red) in the glycerol and ethanol mixture. In figure 6, these data are presented in terms of the traditional Re based on the flow shear rate and the square of the sphere diameter, $Re = \rho d^2 \dot{\gamma}/\mu$, which is the parameter typically used in sheared suspension studies. In terms of Re, the data extends from 0.5 to 50. For all of the solid fractions, the normalised torque is independent of Re below approximately $Re \approx 5$. For $Re \geqslant 5$, the data for $\phi = 40\,\%$ begins

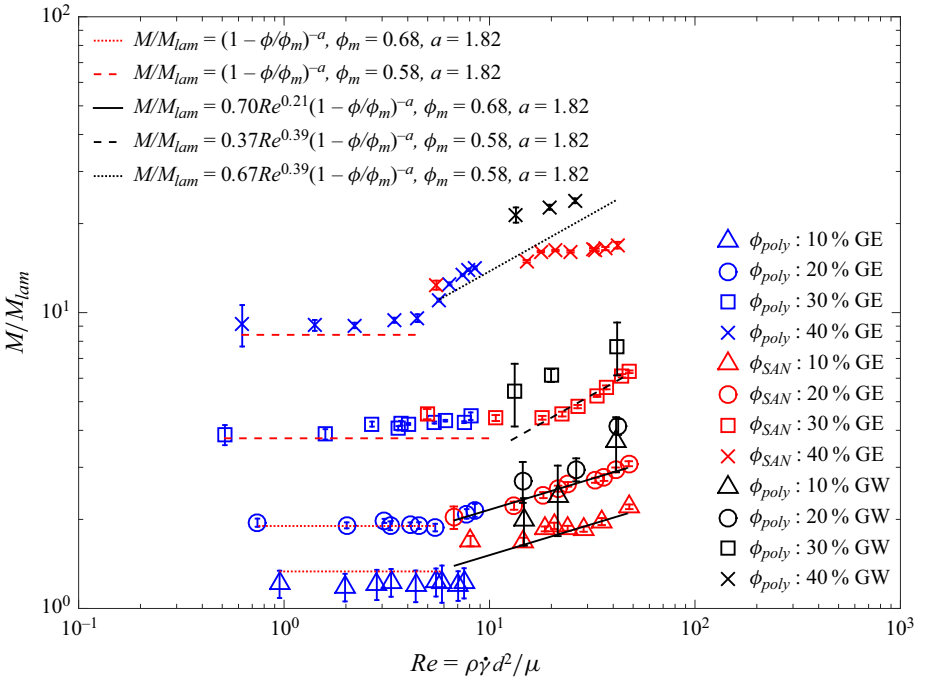

Figure 6. The ratio of the experimental torque measurements, M, to the torque of laminar flow, M_{lam}, in terms of Re, before the transition to turbulence. The figure presents results of small polystyrene particles suspending in 51 % glycerol–ethanol and 18 % glycerol–water mixtures, as well as large SAN particles suspending in 51 % glycerol–ethanol mixture, with $\phi = 0.1$, 0.2, 0.3 and 0.4. The red dotted lines represent the KD relations using $\phi_m = 0.68$ and $a = 1.82$. The dashed lines in red represent the KD relations using $\phi_m = 0.58$ and $a = 1.82$. The black solid lines represent the fitting curves for $\phi = 0.1$ and 0.2. The dashed line in black corresponds to the fitting curve for $\phi = 0.3$. The dotted line in black represents the fitting curve considering $\phi = 0.4$.

to show an increased dependence on Re. The measurements for ϕ from 0.1 to 0.3 show an increased dependence on Re at slightly larger values of Re.

With an increasing Re, the experiments with the same ϕ values show variations depending on the fluids and particles. At ϕ of 0.2, 0.3 and 0.4, the polystyrene measurements (data points in blue) align with the SAN measurements (data points in red) in the liquid mixture of glycerol and ethanol for Re around 10. The polystyrene spheres suspended in the less-viscous fluid (data sets in black), however, fall above the SAN data. For $\phi = 0.1$, the SAN particle (red data sets) at $Re \approx 8$ are larger than the polystyrene (blue data sets) result. As described previously, this difference is attributed to the trapped small-scale polystyrene particles in the interstices of the large particles glued on the rheometer wall. For $Re > 15$, the measurements for the polystyrene spheres in the 18 % glycerol–water mixture lie above the 10 % result for the SAN spheres in the 51 % glycerol–ethanol mixture.

As an alternative to using Re that depends on d^2, figure 7 presents the same M/M_{lam} measurements as found in figure 6 using a modified Reynolds number that depends on d and the maximum speed in the shear flow, $Re' = \rho d U_o/\mu$, where the speed of the outer wall is taken as $U_o = \omega r_o$. As the inertia of the flow increases, prior studies suggest an increase in velocity fluctuations, differences between the solid and fluid velocities and particle collisions, especially in the region near the wall (Zhou & Prosperetti 2020; Yousefi *et al.* 2023). Under these conditions, the appropriate scaling of the stresses may

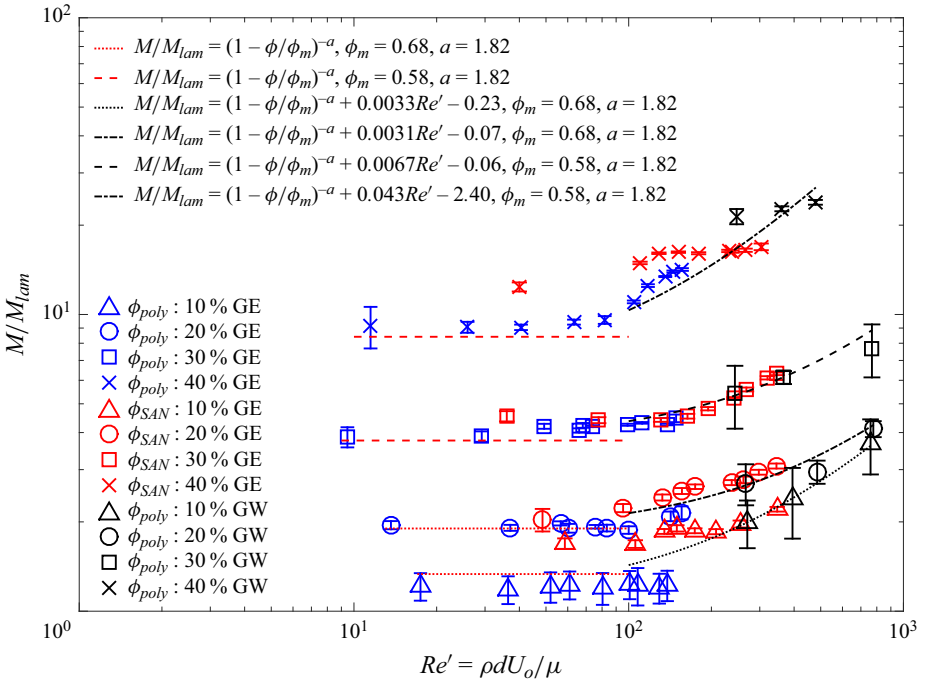

Figure 7. The ratio of experimental torque measurements, M, to the laminar torque, M_{lam}, with respect to Re' before the turbulent transition. The figure presents measurements of small polystyrene particles suspended in 51 % glycerol/49 % ethanol and 18 % glycerol/82 % water mixtures, as well as large SAN particles suspended in 51 % glycerol/49 % ethanol mixture, for $\phi = 0.1$, 0.2, 0.3, and 0.4. The red dotted lines represent the KD relations using $a = 1.82$ and $\phi_m = 0.68$. The dashed lines in red represent the KD relations using $\phi_m = 0.58$ and $a = 1.82$. The black lines correspond to the fitting curves for ϕ from 0.1 to 0.4.

depend on the diameter of the particle and not the square of the particle diameter. In terms of Re', the data extend from 10 to 500. Unlike the results with respect to Re, the data points for different experiments overlap using Re', especially for the 20 %, 30 %, and 40 % solid fractions, as compared with the data presented using Re. The increase in the normalised torque with Re' begins at $Re' \approx 100$. As discussed previously for 10 % solid fraction, the M/M_{lam} values for the SAN particles are greater than for polystyrene particles for $Re' \leqslant 100$. An improvement in using Re' for 10 % is that the data for polystyrene particles in glycerol–water (data sets in black) correspond well with the SAN measurements in high-viscosity fluid mixture (data sets in red), which is not found using Re.

In figures 6 and 7, the relative viscosity using the KD relation is shown for lowest values of either Re or Re'. To compare the use of Re with Re' in modelling the normalised torque below the transition to turbulence, the data in figures 6 and 7 are fit with curves for M/M_{lam} in terms of Re or Re' using the KD model to capture the effect of solid fraction with $\phi_m = 0.68$ for 10 % and 20 % results and $\phi_m = 0.58$ for 30 % and 40 % results. Using Re, the data are best fit using a power law, as found below for $Re \geqslant 10$:

$$M/M_{lam} = a_1 Re^{a_2} \mu_r(\phi, \phi_m), \tag{4.3}$$

where a_1 and a_2 are constants fitted to the data and given in table 1.

Using Re' to correlate the data, the fitted curves involve the KD effective viscosity function, $\mu_r(\phi, \phi_m)$, plus a function that depends linearly on Re' with coefficient, b_1, and a constant b_2, as follows:

$$M/M_{lam} = \mu_r(\phi, \phi_m) + b_1 Re' + b_2. \tag{4.4}$$

The values of b_1 and b_2 are found in the table. Note that the value of b_2 reflects how well the KD model estimates μ_e for low values of Re'. For $\phi \leqslant 0.3$, the largest value of b_2 corresponds with $\phi = 0.1$; as discussed previously, the difference results from the roughened walls.

To quantify how well the models fit with the measurements in figures 6 and 7, table 1 also presents the root-mean-square (r.m.s.) deviations of the experimental measurements from the fitting curves. For $\phi = 10\,\%$, the r.m.s. of the deviation between the experimental results and the fitting model in figure 6 for Re from 10 to 100 is 0.54. The r.m.s. for the same data sets with respect to the fitting model in figure 7 for $100 < Re' < 400$ is 0.17, roughly three times smaller than the r.m.s. number using Re. For $\phi = 20\,\%$, $30\,\%$ and $40\,\%$, the values of r.m.s. in figure 7 are 0.20, 0.40 and 2.91, respectively, which are smaller than the corresponding r.m.s. values in figure 6. Overall, the highest r.m.s. values are for $\phi = 0.4$.

The measurements of M/M_{lam} are further normalised by the KD relation, $\mu_e/\mu = (1 - \phi/\phi_m)^{-a}$ for ϕ from 0.1 to 0.4, and the results are shown with respect to Re' in figure 8. Similar to the normalisation results presented in figures 6 and 7, all the low solid fraction results ($10\,\%$ and $20\,\%$) are normalised by μ_e/μ using ϕ_m of 0.68, while the $30\,\%$ and $40\,\%$ solid fraction results are normalised using ϕ_m of 0.58. For solid fractions less than $30\,\%$ and Re' until 400, the collapsed normalised torques compare well with a fitting curve that includes the inertial contributions:

$$(M/M_{lam})/(\mu_e/\mu) = M/M_e = 1 + 0.002Re', \tag{4.5}$$

where $M_e = 2\pi\mu_e H r_i^2 \dot{\gamma}$. The figure and the curve demonstrate the increase in the normalised torque, M/M_e, as Re' increases. Prior to transition M/M_e starts to increase as the flow inertia is increasing, followed by a further magnitude increase at the fully turbulent state. As described earlier, the $10\,\%$ results immersed in the liquid mixture of ethanol and glycerol lie below the fitting curve. The $40\,\%$ results before the transition to turbulence fall above the fitting curve and show less variation with Re' than found for the lower solid fractions. These differences may result from the different contributions to the bulk stress, such as the Reynolds stresses and particle stress, having different dependencies on Re' and ϕ. The fitting curve also demonstrates that at $Re' = 100$, there is approximately a $20\,\%$ increase in torque as compared with the torque estimated using only the KD relation. At $Re' = 500$, the torque has approximately doubled.

In the fully-turbulent regime for $Re' > 2000$, the collapsed data immersed in the low-viscosity fluid align closely, showing a consistent trend. The data are fit using a power-law relation:

$$(M/M_{lam})/(\mu_e/\mu) = 0.29{Re'}^{0.49}. \tag{4.6}$$

The torque ratio increases with ${Re'}^{0.49}$, which shows a weaker dependence on the rotational speed than found for a pure fluid where the torque ratio increases with $Re_b^{0.66}$ and Re_b depends linearly on ω. Hence, the particles increase the overall torque, but there is a decreased dependence on the rotational speed or shear rate as compared with a fully turbulent flow for a pure fluid. Similar results were found in the study by Linares *et al.* (2017).

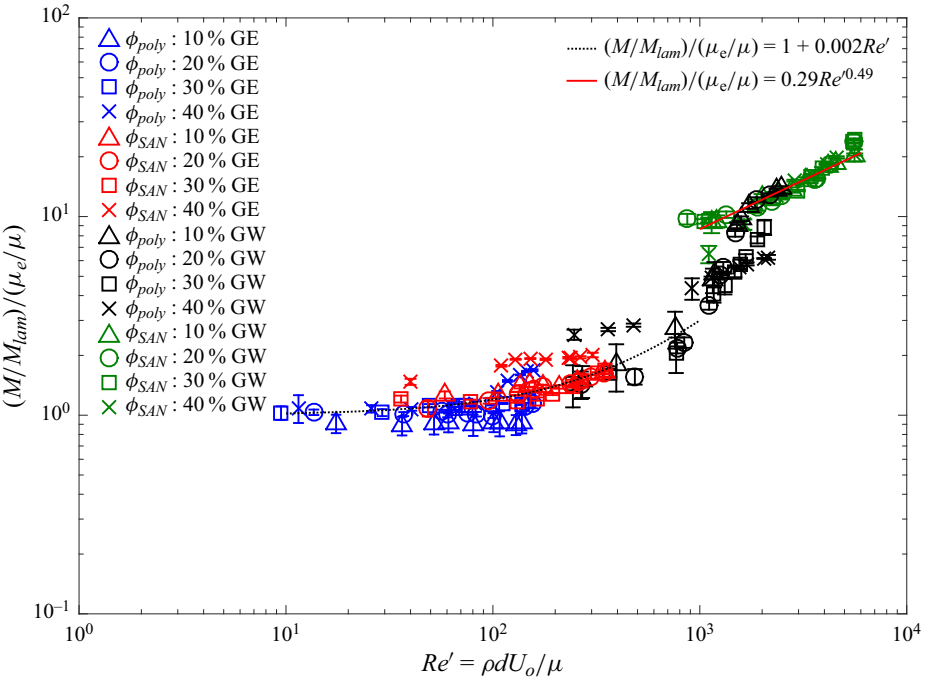

Figure 8. Normalised torque (M/M_m) divided by the KD relation (μ_e/μ) with respect to Re'. The 10 % and 20 % results are normalised by the KD equation considering $\phi_m = 0.68$ and $a = 1.82$. The 30 % and 40 % results are normalised by the KD equation using $\phi_m = 0.58$ and $a = 1.82$. The dotted line in black represents the fitting curve for measurements before the fully turbulent state. The solid line in red is the fitting model for the measurements in the turbulent regime.

As described previously, the experiments for 50 % solid fraction were not conducted at the lowest motor rotational speed because of the stress imparted by the particles on the confining walls when sheared. Using the values of M_o, the data for 50 % are plotted as $(M - M_o)/M_{lam}$ with respect to Re' in figure 9. The M_o values are listed in the figure caption. The values of yield torque, M_o, can be compared to the torque at the lowest shear rate using an effective viscosity calculated using the KD relation for $\phi = 0.5$. Using the minimum, steady-state rotational speed to calculate the corresponding shear rate, $\dot{\gamma}_{min}$, the corresponding torque is calculated as $M_{min,e} = 2\pi\mu_e H r_i^2 \dot{\gamma}_{min}$. For the 50 % solid fraction experiments, the ratio $M_o/M_{min,e}$ ranges from 1 to 6 for the different experiments. Because these values are greater than one, the suspension may not be fully sheared across the width of the annulus at the lowest shear rates. At larger rotational speeds, the particles become more evenly distributed across the annulus.

By plotting the measurements in terms of $(M - M_o)/M_{lam}$, the results of the 50 % polystyrene particles (data points in blue) and SAN particles (data points in red) in the high-viscosity fluids overlap, and the data can be fitted with $(M - M_o)/M_{lam} = 34.6$, which is close to the KD relative viscosity using $\phi_m = 0.58$ as presented in table 1. The two data sets in the glycerol–ethanol fluids compare well for Re' near 100. Hence, the 50 % measurements in the suspending fluids with high viscosity are independent of the particle size, and the corresponding M/M_{lam} values do not depend on Re'. The one exception is the data point at $Re' = 14$, where the error bar is large because of the variations in the motor at the lowest rotational speed. Beyond the laminar–turbulent transition, the 50 %

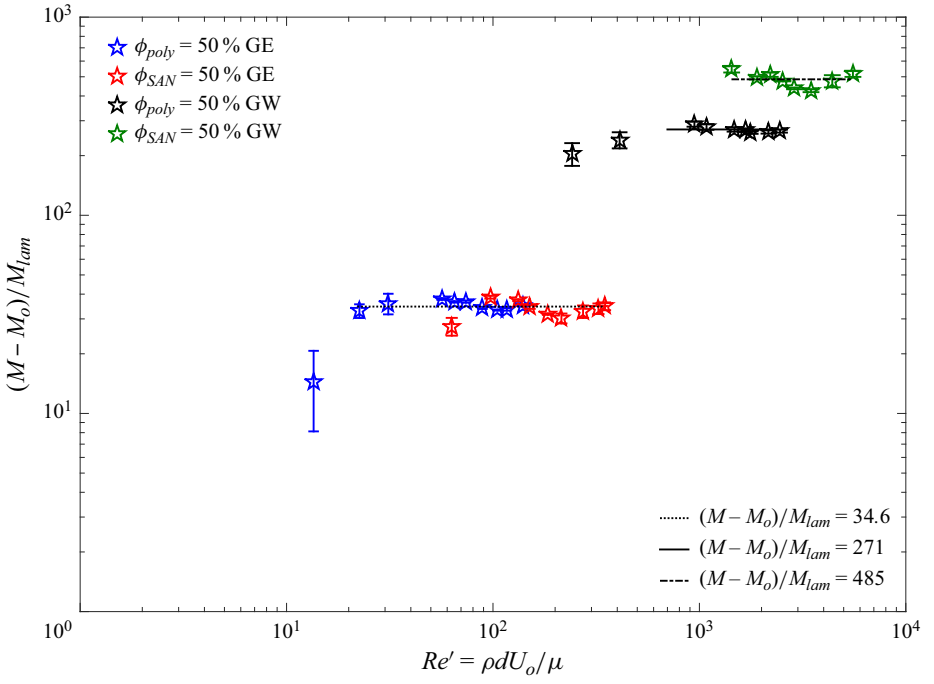

Figure 9. The ratio of $(M - M_o)$, to the laminar flow torque, M_{lam}, with respect to Re' for small polystyrene particles and large SAN particles suspending in the fluid mixtures of 51 % glycerol/49 % ethanol and 18 % glycerol/82 % water considering 50 % solid fraction. Here $(M - M_o)/M_{lam} = 34.6$ is the fitting curve for all particles in the glycerol–ethanol mixture and $(M - M_o)/M_{lam} = 271$ and $(M - M_o)/M_{lam} = 485$ are the fitting curves for polystyrene and SAN particles in glycerol–water mixtures respectively. The values for M_o are 0.35 N m and 0.59 N m for polystyrene particles and SAN particles in the high-viscosity mixture, and are 0.11 N m and 0.14 N m for polystyrene particles and SAN particles in the low-viscosity mixture.

polystyrene measurements using glycerol–water fluids (black data points) can be best fitted with $(M - M_o)/M_{lam} = 271$, which is significantly greater than the corresponding laminar measurements. The substantial difference in the normalised torque before and after the transition for $\phi = 0.5$ results shows the impact of the turbulence. The SAN measurements for $\phi = 0.5$ in the low viscosity (data points in green) can be best fitted with $(M - M_o)/M_{lam} = 485$, which is 1.8 times greater than the corresponding 50 % results of small polystyrene particles in the glycerol–water mixture, indicating the impacts of different levels of turbulence. The earlier work by Linares *et al.* (2017) showed sheared thinning at 50 % solid fraction; however, the value of M_o was not subtracted from the raw data. In the study by Koos *et al.* (2012), the torque ratios were also found to be independent of Re. Those experiments included measurements of the particle slip velocity and inferred a depletion layer with lower solid fraction near the surface. Because the solid fraction must go to zero at the wall, the effective viscosity is lower in this region and the velocity gradient is higher. Although the slip is not measured in the current experiments, the normalised torque measurements at 50 % solid fraction suggest that there may be a region of particle slip and a depletion layer near the wall, even with the increased roughness in the current experiments as compared with the earlier study by Koos *et al.* (2012). Similar results are found in the simulations by Zhou & Prosperetti (2020).

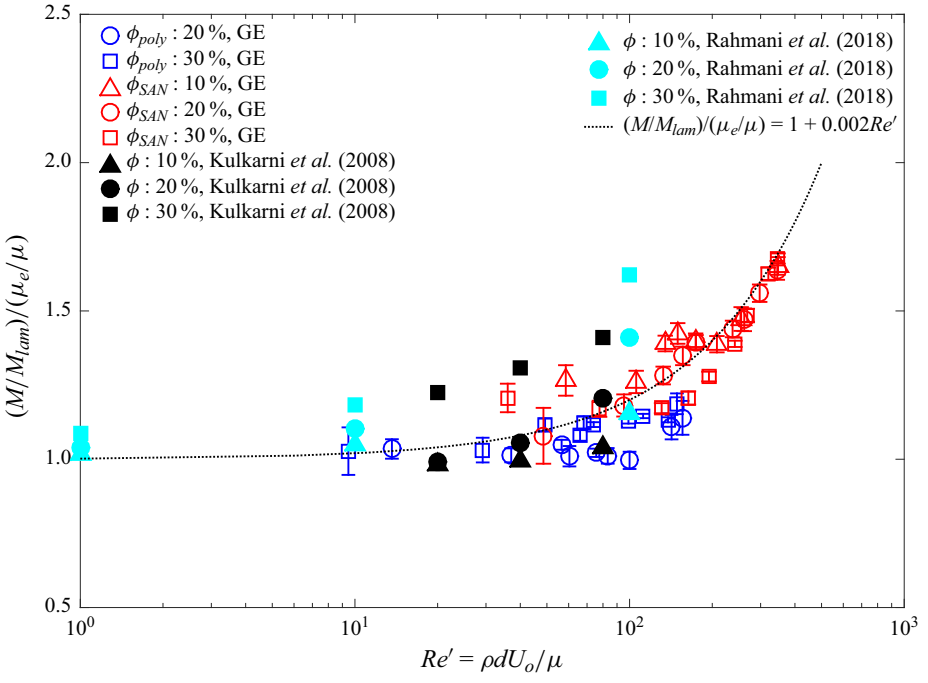

Figure 10. Neutrally buoyant experimental results, M/M_{lam}, and numerical results, normalised by μ_e/μ with respect to Re'. The experimental measurements correspond to small polystyrene particles suspended in high-viscosity liquids (GE) for ϕ from 0.2 to 0.3, as well as large SAN particles in the GE mixture for solid fractions from 0.1 to 0.3. The simulations are from Kulkarni & Morris (2008) and Rahmani *et al.* (2018), with solid fractions from 10 % to 30 %. The 10 % and the 20 % experimental measurements are normalised using $\phi = 0.68$ and $a = 1.82$, while the 30 % experimental results are normalised using $\phi = 0.58$ and $a = 1.82$. The simulations of Kulkarni & Morris (2008) use the Eilers equation with $b = 1.5$ and $\phi_m = 0.58$. The results of Rahmani *et al.* (2018) use the KD relation using $\phi_m = 0.63$ and $a = 1.58$.

5. Discussion and comparison with numerical studies

Figure 10 presents the current measurements in linear scale using polystyrene and SAN particles in the glycerol–ethanol fluids, as well as the numerical results using neutrally buoyant spherical particles from Kulkarni & Morris (2008) and Rahmani *et al.* (2018) in terms of Re'. In these two numerical studies, the three-dimensional flow is generated by the translation of two plates separated by a distance, H, each moving in the opposite directions with speed U; hence, the shear rate in the paper is defined as $\dot{\gamma} = 2U/H$ and Re is related to Re' as $Re' = Re(H/2d)$. In these studies, the shear force along the walls is computed rather than the torque measurement. The spacing between the walls is the same in both studies with $H/d = 10$, which is sufficient to prevent significant banding of particles as demonstrated in the study by Gallier *et al.* (2016). The Caltech experimental apparatus using an outer-rotating cylinder with significant roughness helps to achieve a homogeneous distribution of particles prior to the turbulent transition for $\phi = 0.1$, 0.2 and 0.3, ensuring a similar rheological configuration in comparison to the simulations. Because of the issues previously discussed regarding the polystyrene particles at the 10 % solid fraction in glycerol–ethanol, this data set is not included. Similar to the normalisation in figure 9, the experimental results with lower solid fractions, 10 % and 20 %, are normalised by the KD relation with $\phi_m = 0.68$ and $a = 1.82$, while the 30 % solid fraction result is

normalised using $\phi_m = 0.58$ and $a = 1.82$. For the numerical studies, the stress ratios found in the papers are normalised by the effective viscosity models used in those papers. The work by Kulkarni & Morris (2008) uses the Eilers relation:

$$\mu_e/\mu(\phi) = [1 + b\phi/(1 - \phi/\phi_m)]^2 \tag{5.1}$$

with $\phi_m = 0.58$ and $b = 1.5$. The study by Rahmani *et al.* (2018) uses the KD equation with $\phi_m = 0.63$ and $a = 1.58$.

Both the simulation and experimental measurements show an increased dependence on Re'. For $\phi = 0.1$, the normalised torques from Kulkarni & Morris (2008) and Rahmani *et al.* (2018) align well with the current measurements, as well as the curve of $(M/M')/(\mu_e/\mu) = 1 + 0.002Re'$. For the 20 % fraction, both numerical values show good agreement with the current measurements; at $Re' = 100$, the 20 % result from Rahmani *et al.* (2018) is approximately 18 % greater than the current experimental result. The 30 % numerical results fall above the current measurements, with normalised torques being 20 % and 35 % greater than the corresponding experimental data points for $Re' = 80$ and 100 respectively. There are differences between the simulations and the experiments, such as the wall roughness, the dimensions, and the difference between a shear flow and an annular flow with one moving surface; these effects can impact the local micro-structure of the flows and contribute to differences in the measured stresses.

6. Conclusion

The current study involves neutrally-buoyant suspensions using two particle sizes and two fluid viscosities in the Caltech coaxial rheometer with rough walls; additional experiments involved pure liquids to study the transition to turbulence for the rheometer. With the current experimental set-up, the measurements presented in this study extend the rheological experiments to the important Re regime found in many geological and engineering applications. The conducted measurements on liquid–solid flows cover both dilute and dense solid fractions with ϕ from 10 % to 50 % and particle Reynolds numbers Re between 0.5 and 800, extending from the laminar state to the fully-turbulent state.

For neutrally buoyant particulate flow measurements with Re from 0.5 to 10 and ϕ from 10 % to 40 %, the normalised torque of particulate flows is independent of Re, but increases with ϕ. For Re ranging from 10 to 100 and ϕ less than 40 %, due to the increased inertial effects, the normalised torque depends on Re and the ϕ, showing an enhanced normalised torque as Re increases. As Reynolds number is increased beyond the critical Re_b, the liquid–solid flows using either the polystyrene particles or the SAN particles transition to the turbulent states. For ϕ from 10 % to 30 %, the small polystyrene particles increase μ_e of the suspension and delay the laminar–turbulent transition (Balachandar & Eaton 2010); for ϕ of 40 % and 50 %, the measured torques are greater than for a pure fluid. For the suspension with larger SAN particles, the addition of particles increases the torques for all solid fractions as compared with results for pure fluids. Similar to the studies considering flows in pipes or channels, the combined effects of the increasing Reynolds stress and turbulence level lead to enhanced momentum transport (Yousefi *et al.* 2023). The current experimental results are consistent with prior studies that turbulence can be suppressed or augmented depending on the solid fraction and size of the particle (Gore & Crowe 1989; Matas *et al.* 2003; Yu *et al.* 2013; Leskovec *et al.* 2020).

The Reynolds number based linearly on the diameter of the particle and the maximum velocity of the flow, $Re' = \rho d U_o/\mu$, as traditionally used to examine flow over an isolated sphere, is proposed to correlate the normalised torques before transition and for solid fractions from 10 % to 40 %. New rheological models based on the KD relationship

and Re' are introduced based on the experimental measurements for the Re' regime from 10 to 500. By comparing the r.m.s. values of the fitting models using Re and Re', Re' is proved to be a better scaling variable to correlate the normalised torque of the moderate-Reynolds-number liquid–solid flow before transition than the traditional particle Reynolds number, Re. Interestingly, the use of Re' leads to a simpler expression to correlate the fully turbulent data for $\phi \leqslant 40\,\%$. For $\phi = 50\,\%$, the values of the normalised torques are significantly larger than found for lower values of ϕ and are independent of Re' when presented in terms of $(M - M_o)/M_{lam}$.

Although the current torque measurements and the rheological models based on Re' and KD equations can aid the development of rheological models for moderate-Reynolds-number liquid–solid flows, work still needs to be done to understand the contribution of the particle collisions, the particle stress, and the Reynolds stress on the bulk stresses, especially since each of these terms may depend differently on Re or Re'. Future studies on inertial suspensions should quantify the velocity fluctuation for different values of particle size to gap size, d/b (Brandt & Coletti 2022), and measure the distribution of the velocity and solid fraction (Yousefi *et al.* 2023). As the Stokes number, St, increases, the particle collision may also become increasingly important for the torque measurement (Yang & Hunt 2006; Zhou & Prosperetti 2020). Therefore, direct pressure measurements of the particle collision can help determine the contribution to the stresses in a liquid–solid flow.

Funding. This research is based on work supported by the National Science Foundation (NSF) under grant no. 1706166.

Declaration of interests. The authors report no conflict of interest.

Author ORCIDs.
Melany L. Hunt https://orcid.org/0000-0001-5592-2334.

References

Acrivos, A., Fan, X. & Mauri, R. 1994 On the measurements of the relative viscosity of suspensions. *J. Rheol.* **38** (5), 1285–1296.

Agrawal, N., Choueiri, G.H. & Hof, B. 2019 Transition to turbulence in particle laden flows. *Phys. Rev. Lett.* **122**, 114502.

Bagnold, R.A. 1954 Experiments on gravity-free dispersion of large solid spheres in a Newtonian fluid under shear. *Proc. R. Soc. Lond.* A **225**, 49–63.

Balachandar, S. & Eaton, J.K. 2010 Turbulent dispersed multiphase flow. *Annu. Rev. Fluid Mech.* **42** (1), 111–133.

Barnes, H.A. 1995 A review of the slip (wall depletion) of polymer solutions, emulsions and particle suspensions in viscometers: its cause, character, and cure. *J. Non-Newtonian Fluid Mech.* **56** (3), 221–251.

Batchelor, G.K. 1970 The stress system in a suspension of force-free particles. *J. Fluid Mech.* **41**, 545–570.

Boyer, F., Guazzelli, E. & Pouliquen, O. 2011 Unifying suspension and granular rheology. *Phys. Rev. Lett.* **107**, 188301–5.

Brandt, L. & Coletti, F. 2022 Particle-laden turbulence: progress and perspectives. *Annu. Rev. Fluid Mech.* **54** (1), 159–189.

Cartellier, A. & Riviere, N. 2001 Effect of particle size on modulating turbulent intensity. *Phys. Fluids* **13**, 2165–2181.

Cheng, N. 2008 Formula for the viscosity of a glycerol–water mixture. *Ind. Engng Chem. Res.* **47**, 3285–3288.

Coles, D. 1965 Transition in circular Couette flow. *J. Fluid Mech.* **21**, 385–424.

Coles, D. & VanAtta, C. 1966 Measured distortion of a laminar circular Couette flow by end effects. *J. Fluid Mech.* **25**, 513–521.

Dash, A., Anantharaman, A. & Poelma, C. 2020 Particle-laden Taylor–Couette flows: higher order transitions and evidence for azimuthally localized wavy vortices. *J. Fluid Mech.* **903**, A20.

ELLENBERGER, J. & FORTUIN, J.M.H. 1985 A criterion for purely tangential laminar flow in the cone-and-plate rheometer and the parallel-plate rheometer. *Chem. Engng Sci.* **40**, 111–116.

ERNST, R.C., WATKINS, C.H. & RUWE, H.H. 1936 The physical properties of the ternary system ethyl alcohol-glycerin-water. *J. Phys. Chem.* A **40**, 5.

GALLIER, S., LEMAIRE, E., LOBRY, L. & PETERS, F. 2016 Effect of confinement in wall-bounded non-colloidal suspensions. *J. Fluid Mech.* **799**, 100–127.

GORE, R.A. & CROWE, C.T. 1989 Effect of particle size on modulating turbulent intensity. *Intl J. Multiphase Flow* **15**, 279–285.

HADDADI, H. & MORRIS, J.F. 2014 Microstructure and rheology of finite inertia neutrally buoyant suspensions. *J. Fluid Mech.* **749**, 431–459.

HUNT, M.L. & ZENIT, R. 2024 Beyond Bagnold: rheological measurements of inertial suspensions. *Intl J. Multiphase Flow* (submitted).

HUNT, M.L., ZENIT, R., CAMPBELL, C.S. & BRENNEN, C.E. 2002 Revisiting the 1954 suspension experiments of R.A. Bagnold. *J. Fluid Mech.* **452**, 1–24.

IVERSON, R.M. 2012 Elementary theory of bed-sediment entrainment by debris flows and avalanches. *J. Geophys. Res.* **117** (F03006), 1–17.

KOOS, E., LINARES-GUERRERO, E., HUNT, M.L. & BRENNEN, C.E. 2012 Rheological measurements of large particles in high shear rate flows. *Phys. Fluids* **24**, 013302.

KULKARNI, P.M. & MORRIS, J.F. 2008 Suspension properties at finite Reynolds number from simulated shear flow. *Phys. Fluids* **20**, 40602.

LARSON, R.G. 1999 *The Structure and Rheology of Complex Fluids*. Oxford University Press.

LASHGARI, I., PICANO, F., BREUGEM, W. & BRANDT, L. 2014 Laminar, turbulent, and inertial shear-thickening regimes in channel flow of neutrally buoyant particle suspensions. *Phys. Rev. Lett.* **113**, 254502.

LESKOVEC, M., LUNDELL, F. & INNINGS, F. 2020 Pipe flow with large particles and their impact on the transition to turbulence. *Phys. Rev. Fluids* **5**, 112301.

LINARES, E., HUNT, M. & ZENIT, R. 2017 Effects of inertia and turbulence on rheological measurements of neutrally buoyant suspensions. *J. Fluid Mech.* **811**, 525–543.

MAJJI, M.V. & MORRIS, J.F. 2018 Inertial migration of particles in Taylor–Couette flows. *Phys. Fluids* **30**, 033303.

MATAS, J.P., MORRIS, J.F. & GUAZZELLI, E. 2003 Transition to turbulence in particulate pipe flow. *Phys. Rev. Lett.* **90** (1), 014501.

MENDEZ-DIAZ, S., SERRANO-GARCIA, J.C., ZENIT, R. & HERNANDEZ-CORDERO, J.A. 2013 Power spectral distributions of pseudo-turbulent bubbly flows. *Phys. Fluids* **25**, 043303.

MOAZZEN, M., LACASSAGNE, T., THOMY, V. & BAHRANI, S.A. 2022 Torque scaling at primary and secondary bifurcations in a Taylor–Couette flow of suspensions. *J. Fluid Mech.* **937**, A2.

OSIPTSOV, A.A. 2017 Fluid mechanics of hydraulic fracturing: a review. *J. Petrol. Sci. Engng* **156**, 513–535.

PICANO, F., BREUGEM, W.P., MITRA, D. & BRANDT, L. 2013 Shear thickening in non-Newtonian suspensions: an excluded volume effect. *Phys. Rev. Lett.* **111**, 98302.

RAHMANI, M., HAMMOUTI, A. & WACHS, A. 2018 Momentum balance and stresses in a suspension of spherical particles in a plane Couette flow. *Phys. Fluids* **30**, 043301.

RAMESH, P., BHARADWAJ, S. & ALAM, M. 2019 Suspension Taylor–Couette flow: co-existence of stationary and travelling waves, and the characteristics of Taylor vortices and spirals. *J. Fluid Mech.* **870**, 901–940.

RAVELET, F., DELFOS, R. & WESTERWEEL, J. 2010 Influence of global rotation and Reynolds number on the large-scale features of a turbulent Taylor–Couette flow. *Phys. Fluids* **22**, 055103.

SAVAGE, S.B. & MCKEOWN, S. 1983 Shear stresses developed during rapid shear of concentrated suspensions of large spherical particles between concentric cylinders. *J. Fluid Mech.* **127**, 453–472.

SCHLICHTING, H. 1951 *Boundary Layer Theory*, 7th edn. McGraw Hill.

SONG, Y. 2022 Rheological measurements in moderate Reynolds number liquid–solid flows. PhD thesis, California Institute of Technology.

STICKEL, J.J., KNUTSEN, J.R., LIBERATORE, M.W., LUU, W., BOUSFIELD, D.W., KLINGENBERG, D.R., SCOTT, C.T., ROOT, T.W., EHRHARDT, M.R. & MONZ, T.O. 2009 Rheology measurements in a biomass slurry: an inter-labotory study. *Rheol. Acta* **48**, 1005–1015.

STICKEL, J.J. & POWELL, R.L. 2005 Fluid mechanics and rheology of dense suspensions. *Annu. Rev. Fluid Mech.* **37** (1), 129–149.

TAPIA, F., ICHIHARA, M., POULIQUEN, O. & GUAZZELLI, E. 2022 Viscous to inertial transition in dense granular suspension. *Phys. Rev. Lett.* **129**, 078001.

TAYLOR, G.I. 1936*a* Fluid friction between rotating cylinders, I. Torque measurements. *Proc. R. Soc. Lond.* A **157** (892), 546–564.

TAYLOR, G.I. 1936*b* Fluid friction between rotating cylinders, II. Distribution of velocity between concentric cylinders when outer one is rotating and inner one is at rest. *Proc. R. Soc. Lond.* A **157** (892), 565–578.
VANATTA, C. 1966 Exploratory measurements in spiral turbulence. *J. Fluid Mech.* **25**, 495–512.
YANG, F.L. & HUNT, M.L. 2006 Dynamics of particle-particle collisions in a viscous liquid. *Phys. Fluids* **18**, 121506.
YEO, K. & MAXEY, M.R. 2013 Dynamics and rheology of concentrated, finite-Reynolds-number suspensions in a homogeneous shear flow. *Phys. Fluids* **25**, 533303.
YOUNG, A.B., SHETTY, A. & HUNT, M.L. 2024 Flow transitions and effective properties in multiphase Taylor–Couette flow. *J. Fluid Mech.* **983**, A14.
YOUSEFI, A., COSTA, P., PICANO, F. & BRANDT, L. 2023 On the role of inertia in channel flows of finite-size neutrally-buoyant particles. *J. Fluid Mech.* **955**, A30.
YU, Z., WU, T., SHAO, X. & LIN, J. 2013 Numerical studies of the effects of large neutrally buoyant particles on the flow instability and transition to turbulence in pipe flow. *Phys. Fluids* **25**, 043305.
ZHOU, G. & PROSPERETTI, A. 2020 Inertial effects in a shear flow of fluid particle mixture: resolved simulations. *Phys. Rev. Fluids* **5**, 0803401.